Title

Size and oxidation state tracking of dynamic Rh catalysts on rutile TiO 2 by ambient-pressure XPS

Journal

Journal of Materials Chemistry A

ISSN

2050-7488

Authors

Gericke, Sabrina M
Erbez, Jake
Chen, Xiaobo
et al.

Publication Date

2026-07-15

DOI

10.1039/d6ta02069k

ARTICLE

Size and Oxidation State Tracking of Dynamic Rh Catalysts on Rutile TiO_2 by Ambient-Pressure XPS

Received 00th January 20xx,
Accepted 00th January 20xx

DOI: 10.1039/x0xx00000x

Sabrina M. Gericke[a], Jake Erbez[b], Xiaobo Chen[c], Anastassiya Khan[d], Zhihengyu Chen[d], Yonghyuk Lee[b,‡], Seunghwa Hong[e], Jake Heinlein[f], Emily K. Schroeder[e], Selin Bac[e], Jonathan Novak[a], Monika Blum[g,h], Slavomir Nemšák[g], Phillip Christopher[e], Matteo Cargnello[f], Adam S. Hoffman[d], Simon R. Bare[d], Samuel Tenney[a], Judith C. Yang[a,c], Anastassia N. Alexandrova[b], Ashley R. Head[a,*]

Rhodium supported on titania (Rh/TiO_2) is an active catalyst for the reverse water gas shift reaction, yet the nature of the active sites for this reaction and others remain under debate. Single atom Rh sites have frequently been proposed as key sites, making it essential to monitor size changes of Rh species under *in situ* conditions to establish the structure–function relationship. However, surface-sensitive *in situ* measurements of nanosized particles remain experimentally challenging and have focused on metal oxide single crystal model systems. Here, we apply ambient pressure X-ray photoelectron spectroscopy (APXPS) to Rh/TiO_2 powdered catalysts under oxidizing and reducing environments. We find size-dependent charge transfer between the Rh and the titania cause binding energy shifts in both oxidized and reduced Rh species. By deconvoluting this effect from oxidation state core level shifts, APXPS can provide qualitative evidence of Rh cluster size changes. The electronic effects responsible for these shifts are explored with density functional theory calculations. *Ex situ* transmission electron microscopy gives insight into particle size while Raman spectroscopy identifies Rh oxide phases. Correlative X-ray absorption spectroscopy and pair distribution function (PDF) measurements confirm the structural changes in the APXPS results. These findings offer direct insight into the dynamic behavior of Rh catalyst sintering and fragmentation based on core-level shifts.

Introduction

The characterization of catalysts under *in situ* conditions is a critical step in understanding their structure-activity relationships. Rhodium (Rh) catalysts supported on titanium dioxide (TiO_2) have gained significant attention due to their catalytic properties in a variety of reactions, such as hydrogenation reactions [1, 2, 3], the reverse water gas shift (RWGS) reaction [4, 5], low-temperature CO oxidation [6, 7], and NO_x removal [6]. However, a comprehensive understanding of the active sites and metal-support interactions remains the subject of scientific debate. Central to this debate is the dynamic nature of Rh species, specifically regarding the size-dependent behavior and stability. In particular, Rh single-atom catalysts (SACs) have been proposed as active sites for the reverse water-gas shift (RWGS) reaction, offering high activity and selectivity [5, 4]. However, Rh in this system is known to be dynamic: single atoms can sinter into particles and particles can disperse to single atoms. [8, 9] To better understand the catalyst's behavior, it is essential to monitor changes in Rh particle size and possible sintering of Rh SACs under *in situ* conditions.

While IR spectroscopy allows single atom identification through the adsorption of CO as a probe molecule [10, 11, 12, 13], such studies are limited by the desorption temperature of CO, therefore limiting its application for *in situ* measurements of Rh SACs. Additionally, CO has been reported to induce fragmentation of Rh particles [14], which highlights the need for an alternative technique with the ability to identify Rh single atoms without altering the structure of the catalyst. Techniques such as X-ray diffraction (XRD) [15] and X-ray scattering [16] typically require crystalline and/or large particles, limiting their applicability for small clusters of Rh species, reported as the most relevant one for catalytic activity. Environmental transmission electron microscopy (ETEM) offers high spatial resolution and the ability to directly observe small particles, but it only probes a limited number of particles at a time. [17]

[a] Center for Functional Nanomaterials, Brookhaven National Laboratory, Upton, New York 11973, USA
[b] Department of Chemistry and Biochemistry, University of California, Los Angeles 90095, USA
[c] Department of Chemical and Petroleum Engineering, University of Pittsburgh, Pittsburgh, Pennsylvania 15261, USA
[d] SSRL, SLAC National Accelerator Laboratory, Menlo Park, California, 94025, USA
[e] Department of Chemical Engineering, University of California, Santa Barbara, California 93106, USA
[f] Department of Chemical Engineering, Stanford University, Stanford, California 94305, USA
[g] Advanced Light Source (ALS), Lawrence Berkeley National Laboratory, Berkeley, California 94720, USA
[h] Chemical Sciences Division, Lawrence Berkeley National Laboratory, Berkeley, California 94720, USA
† Present address: Department of Chemical and Biochemical Engineering, Dongguk University, Seoul 04620, Republic of Korea.

X-ray photoelectron spectroscopy (XPS) is a complementary, surface-sensitive technique, that can characterize the structure and chemical speciation of Rh species, averaging over millimeters of sample area. Prior studies on metallic Rh clusters supported on TiO_2 single crystals have reported shifts in XPS binding energies (BE) as a function of Rh cluster size. [18] These charge-transfer–induced shifts, arising from metal–support interactions between Rh and TiO_2, can reach up to 1 eV, complicating the reliable assignment of oxidation states. In the single-atom regime, variations in the coordination environment of individual Rh atoms can likewise lead to differences in binding energy. For example, two distinct Rh coordination environments have been identified on Fe_3O_4(110). [19, 20] On this surface, Rh single atoms can either bind as a Rh adatom (Rh_{ad}) coordinated to two oxygen atoms or in an octahedral coordination integrated in the surface (Rh_{oct}). These two coordination environments of the Rh single atom can be distinguished by the Rh 3d core level binding energy in XPS: 308.2 eV for the Rh_{ad} and 309.5 eV for the Rh_{oct}. The studies show that the binding energy shifts can serve as sensitive probes for Rh morphology and coordination.

Beyond insight into the Rh bonding environment, binding energies from XPS can identify the Rh oxidation state. Surface science studies of Rh single crystals and thin films report that Rh is stable as rhodium metal Rh^0, Rh_2O_3 (Rh^{3+}) and RhO_2 (Rh^{4+}). [21] While the reported binding energies of 307.2 eV for metallic Rh and 308.3 eV for Rh_2O_3 are quite consistent throughout the literature, [22, 21] the reports for RhO_2 differ considerably. Some authors report that RhO_2 has a binding energy only a few tenths of eV higher than Rh_2O_3, [23] while others report it between 309.0 eV to 310.0 eV [24]. RhO_2 shows discrepancies in literature regarding its binding energy which may arise from difficulties in obtaining pure RhO_2 and maintaining its stability during XPS measurements since it is the least stable of the Rh oxides and thus [25] requiring high O_2 pressures to remain stable under measurement conditions [26]. Some authors report on the observation of satellite features around 311 eV, [24] while other authors did not report observing such features. [23] Overall, these inconsistencies in the literature highlight the challenges in reliably assigning Rh oxidation states in XPS analysis.

As discussed above, the situation gets more complex when small amounts of Rh are deposited on oxide support materials, where the Rh forms nanoscale structures with a size range from isolated Rh atoms to small Rh clusters and to larger nanoparticles. The Rh nanostructures experience a charge exchange with the support material which results in changes of the measured core level shifts making the assignment of Rh oxidation states by XPS measurements challenging. For metallic Rh particles on TiO_2 single crystals, shifts in Rh binding energy of close to 1 eV have been shown to be a function of Rh particle size. [18] Metallic Rh on polycrystalline powder TiO_2 has been reported between 306.6 eV and 307.5 eV [27, 10, 28, 29, 30] and RhO_x was observed between 309.1 eV and 312.8 eV [28, 29, 30]. The variety of reported Rh 3d binding energies for a single oxidation state coupled with possible core level shifts related to Rh structure necessitate a thorough study to deconvolute the two phenomena.

Instrumental developments over the last decades have extended the pressure range of XPS measurements [31]. Modern ambient pressure XPS (APXPS) instruments allow for measurements at pressures of a few mbar and specialized sample holders and setups have been reported to extend the feasible pressure range even further [32, 33], making the technique suitable for *in situ* studies over a broad pressure range. Changing oxidation states during *in situ* measurements increases the complexity of deconvoluting oxidation state core level shifts and shifts resulting from changes in Rh structure discussed above.

In this work, we couple density functional theory (DFT) calculations, *ex situ* transmission electron microscopy (TEM) measurements of Rh particle size, *ex situ* Raman spectroscopy data of Rh oxidation state and *ex situ* PDF measurements of catalyst local structures with *in situ* Rh 3d binding energies from APXPS. Through a series of reference measurements, we deconvolute core-level shifts associated with Rh particle size and oxidation state. Our results demonstrate that the binding energy shifts observed with APXPS can be used to track size differences and changes in both metallic and oxidized Rh species supported on polycrystalline rutile TiO_2 powder at elevated pressures. Furthermore, we show that the formation of Rh SACs in a CO atmosphere can be followed directly using APXPS. Correlative X-ray absorption spectroscopy (XAS) results indicate Rh particle dispersion and SACs formation. These findings establish APXPS as a valuable tool for *in situ* monitoring of Rh particle size changes and dispersion on polycrystalline TiO_2, with implications for understanding catalyst deactivation pathways in RWGS and related reactions.

Experimental Section

Catalyst synthesis

This manuscript discusses the properties of two types of catalysts referred to as WI and NP catalysts. The WI catalysts with nominal Rh weight loadings of 0.1, 0.25, 0.5, 1, and 5 wt.% were synthesized via wetness impregnation, following a previously reported procedure. [5] Typically, rutile TiO_2 support (99.9+% rutile, average particle diameter of 30 nm, US Research Nanomaterials Inc. #US3520) was suspended in HPLC-grade H_2O with stirring at 200 rpm in a ceramic evaporating dish at room temperature. The Rh precursor was prepared separately by dissolving the appropriate amount of Rh(III) nitrate hydrate (Sigma-Aldrich, ~36% Rh basis) in HPLC-grade H_2O. Catalyst batches were synthesized on a 1-2 g scale using a consistent a solid to liquid ratio of 12 g TiO_2/L H_2O, with 20% of the total H_2O volume used for Rh precursor solution and remaining 80% for suspending the TiO_2 support. The Rh precursor solution was introduced into the TiO_2 solution at 0.5 mL/min using a syringe pump under stirring at room temperature. After addition, the solution was heated on a hot plate at 373 K under constant stirring to evaporate H_2O, then further dried in an oven overnight at 373 K. The resulting powder was lightly ground

with a mortar and pestle and calcined in a tube furnace under dry air at 673 K for 4 h with a ramp rate of 10 K/min.

Rhodium nanoparticles (NPs) were synthesized as described in previous work. [34] Typically, $RhCl_3$ (41.8 mg), PVP (MW = 55,000, 222 mg), glucose (720 mg), and KBr (71.4 mg) were added in 10 mL of water to a pressure flask (Ace Glass Inc.). The flask was sealed, and the solution was heated to 140 °C for 3 hours under magnetic stirring. The nanoparticles were subsequently washed in water and separated via precipitation using an acetone antisolvent with centrifugation three times before being dispersed and stored in water. The washing step was performed to ensure the removal of Cl from the catalysts. A thermogravimetric analysis (TGA) was performed to determine the Rh NP concentration in the solution.

The Rh NPs were supported onto the rutile TiO_2 following an antisolvent-induced adsorption method. [35] Briefly, rutile TiO_2 (500 mg) was dispersed in water (5 mL) and sonicated for 5 min. The Rh NP solution was added (the volume was calculated to achieve the desired weight loading) and the solution was stirred for at least 5 min. Next, acetone was added dropwise until precipitation occurred (final acetone:H_2O ~ 3:1, v/v). The precipitate was collected via centrifugation and dried overnight at 80 °C. The sample was then collected, sieved below 180 µm grain size, and calcined at 500 °C for 3 hours. The higher calcination temperature was required to remove residual organic ligands. All chemicals for the synthesis of the NPs were purchased from Sigma-Aldrich and the rutile TiO_2 was purchased from US-Nano (TiO_2, rutile, high purity, 99.9+%, 30 nm).

APXPS measurements

The APXPS experiments were conducted at the Center for Functional Nanomaterials (CFN), Brookhaven National Laboratory, Upton NY, and at the 9.3.2 beamline [36] at the Advanced Light Source (ALS) at Lawrence Berkeley National Laboratory, Berkeley, CA. The CFN system utilized a SPECS Phoibos 100 MCD analyzer for XPS measurements, [37] coupled with a monochromatic Al Kα X-ray source (1486.6 eV, ~ 0.25 eV line width), focused to a spot size smaller than 300 µm. At the ALS, the X-ray spot size is ~1 mm^2 and a linewidth of ~0.2 eV throughout the available energy range. At both setups, the temperature was monitored using a K-type thermocouple.

Due to the insulating nature of the TiO_2 powder, steps were taken to minimize charging effects in the APXPS measurements;., the conductivity of the sample was improved by pressing a small amount of catalyst into a thin pellet anchored onto a tantalum (Ta) foil. The Ta foil was subsequently mounted onto the sample holder. Heating and dosing gases further mitigated charging effects, which were often on the order of 1 to 2 eV. The spectra were binding energy calibrated to the main Ti 2p peak which was adjusted to 459.3 eV. TiO_2 can undergo chemistry or be affected by the Rh electronic structure; however, the amount of Rh is small compared to the amount of TiO_2, and the calibration method has proven reproducible over many experiments, conditions, and XPS instruments. Furthermore, the relative position of all elements was found to be consistent (i.e. there is no differential charging across the binding energy scale). For the lab XPS data and the 880 eV synchrotron data, the spectra could be directly calibrated to the Ti 2p spectrum. This direct calibration was not possible for the 480 eV synchrotron spectra. Instead, these spectra were calibrated by collecting Ti 2p and C 1s spectra at 880 eV as well as Rh3d and C 1s with 480 eV. The C 1s spectrum at 880 eV was calibrated to the Ti 2p at 880 eV. Subsequently the C1s at 480 eV was calibrated to the C 1s at 880 eV and used to calibrate the Rh 3d at 480 eV. A Shirley background was subtracted from all spectra. Details about the peak shape, intensity ratio and position can be found in the SI. The APXPS spectra were fitted using the Casa XPS software. [38]

DFT calculations

Spin polarized DFT calculations were performed using the Vienna Ab initio simulation package (VASP) using the projector augmented wave method [39]. The valence states of Rh (4p, 4d, 5s), O (2s, 2p), Ti (3p, 3d, 4s), and C (2s, 2p) were modeled with a plane wave basis set at an energy cutoff of 500 eV. Electronic exchange and correlation were calculated using the semi-local generalized gradient approximation and the Perdew-Burke-Ernzerhof (PBE) functional [40]. To account for strongly correlated electrons of the Ti ions, the DFT+U correction was applied to the Ti 3d electrons [41]. A Hubbard parameter of 3.5 eV has been shown to be effective for structural optimization, and for a more accurate description of localized Ti 3d states, a larger Hubbard parameter of 4.0 eV was used to compute CLS [42, 43]. Due to the large size of the unit cells, a Monkhorst-Pack (1 x 1 x 1) gamma centered k-point grid was used. XAS spectra were computed by the super-cell core-hole method (ICORELEVEL = 2) available in VASP [44]. All simulated CLS were calculated relative to the metallic Rh 3d core binding energy with an experimentally determined value of 307.2 eV [22, 21]. CLS were calculated via CLS = $(E_{ex} - E_{ex,ref}) - (E_{ground} - E_{ground,ref})$ where $E_{ex,ref}$ and $E_{ground,ref}$ are the excited and ground state energies of the metallic Rh 3d electrons, respectively.

For fast screening of configurations, a trained machine learning potential (MLP) was used to identify GM structures and results were refined with DFT. The MLP was implemented by the MACE architecture [45, 46]. Training consisted of an active learning procedure that converged energy RMSE, force RMSE, and committee uncertainty [47]. Data displaying accuracy of the trained MLP is available in the supporting information. All calculations were performed on a 4x2 rutile TiO_2(110) periodic slab with four tri-layers with the bottom two tri-layers fixed. A vacuum layer of at least 10 Å was always maintained. Grand canonical optimization of surfaces under reactive conditions was carried out using GOCIA [48]. For possible $RhTiO_x$, structures, 650 structures were generated and evaluated. For metallic Rh clusters of each size, 100 different structures were generated and evaluated. For grand canonical optimization of CO coverage on metallic Rh clusters, at least 1000 structures were generated for each size. For potential locations of the Rh *gem*-dicarbonyl, 100 structures were generated and evaluated.

Raman measurements

The Raman measurements were collected on a Photothermal Spectroscopy Corp. mIRage + Raman system

purged with dry nitrogen. The Raman system utilized a 0.78 numerical aperture along with a 532 nm laser with a power of 450 mW. The laser power was reduced through a series of filters to 2.7% to an equivalent power of 12.15 mW. Raman spectra were co-averaged over 1000 scans.

TEM experiments

HAADF-STEM imaging of Rh/TiO_2 catalysts was conducted *ex situ* at multiple magnifications using a Hitachi HD2700C scanning transmission electron microscope equipped with a probe corrector and operated at 200 kV.

PDF measurements

High-energy X-ray scattering experiment (λ = 0.1665 Å) was performed at beamline 28-ID-1, National Synchrotron Light Source II, Brookhaven National Laboratory on pure rutile TiO_2 and Rh/TiO_2 catalyst prepared by wetness impregnation with Rh loading from 0.1 wt% to 5 wt%. Samples were packed in 1 mm OD Kapton capillaries. Two-dimension scattering patterns were calibrated using a CeO_2 standard and integrated with GSAS-II. [49] PDFs were extracted via PDFgetX2, [50] with a *Q* range = 0.5 to 24.0 $Å^{-1}$. Non-negative matrix factorization was applied to the PDFs in the *r*-range of 1 to 5 Å. Tests with different numbers of components showed a two-component NMF analysis was sufficient to describe the whole datasets. [51, 52]

XAS measurements.

X-ray absorption spectra were collected at beamline 10-2ES2 at the Stanford Synchrotron Radiation Light source at the SLAC National Accelerator Laboratory. Beamline 10-2 is a center station on a wiggler source equipped with a liquid-nitrogen cooled double-crystal Si (111) phi = 90° monochromator. The monochromator was fully tuned allowing for harmonics to pass through. The maximum intensity of the harmonic beam was detuned 30% at 500 eV above the Rh K-edge (23,220 eV) to minimize the effects of the 3rd harmonics. The incident and transmitted X-ray beam was detected using Ar-filled ionization chamber operated at 700 VDC and negative polarity. The X-ray beam size was 0.3 mm [V] x 2.5 mm [H]. Rh K-edge XAS spectra of the samples were collected in fluorescence geometry using a PIPS detector. A Rh metal foil (25 um thickness) was scanned simultaneously in transmission geometry as an internal energy standard. Extended X-ray absorption fine structure (EXAFS) spectra were collected from 200 eV below the Rh K-edge to the wave vector k = 15 $Å^{-1}$. XAS spectra were aligned, calibrated, and normalized using the Athena interface of the Demeter software package. [53] The Artemis interface was used for fitting EXAFS data, using the crystal structure of Rh metal and orthorhombic Rh_2O_3 (Pbca, a=5.14 Å, b=5.44 Å, c=14.69 Å) (ICSD-9206) to produce Rh-Rh and Rh-O scattering paths respectively. For the Rh–CO model, single-scattering (Rh–C, Rh–O) and multiple-scattering (Rh–C–O, Rh–C–O–C) paths were generated using the $Ir(CO)_2(acac)$ crystal structure, with the Ir atom substituted by Rh during FEFF calculations in Artemis. EXAFS fits were performed using a k-range of 3.0–12.0 $Å^{-1}$ and a R-range of 1–3 Å. An amplitude correction factor of $S_0^2 = 0.85$ was calculated by fitting bulk Rh foil (Table S4, Figure S4).

5.5 mg of catalyst was pressed, sieved (80–125 µm), and loaded into a 1 mm OD x 0.96 mm ID quartz capillary (Hilgenberg) forming a packed bed approximately 0.6 cm long held between plugs of quartz wool. The capillary was installed in a custom-built in-situ flow cell. [54] The process gases were controlled by mass flow controllers (Brooks Instruments). The sample was heated using resistive heaters placed above and below the catalyst bed, and their temperature was controlled by a PID controller with a thermocouple placed in contact with the upper heater. The temperature of the catalyst bed was measured by second thermocouple which was in contact with the quartz wool plug of the outlet side of the catalyst bed.

The experiment was performed using the following protocol: first, the sample was exposed to oxidative pretreatment by heating from RT to 400°C at 16 °C/min in flowing 20% O_2/He (20 sccm), dwelling for 30 minutes at temperature, cooling down to RT (less than 40°C), and purging with flowing He. Next, the catalyst was reduced by heating from RT to 400 °C at 16°C/min under flowing H_2, dwelling for 30 min at 400 °C, cooling to 80 °C, and purging with He. Finally, the sample was exposed to 10% CO/He for 1 hour, cooled to RT, and purged with He.

Results

***Ex situ* characterization**

In this work, we studied six catalysts with varying size distributions of Rh nanoparticles. Five catalysts with different nominal Rh loading (5 wt%, 1 wt%, 0.5 wt%, 0.25 wt% and 0.1 wt%) were prepared using the wetness impregnation (WI) method, and one catalyst was prepared using 1 wt% of aqueous-phase synthesis for size-controlled Rh nanoparticles (NP). The last step of the synthesis includes a calcination in O2 at 400 °C for the WI catalysts and at 500 °C for the NPs. Figure 1 shows TEM images of the catalysts showing the different sizes of the Rh particles post synthesis. The TEM images in Figures 1a-e show that the size of the Rh particles on the WI catalysts decreases with decreasing Rh loading. We have analyzed the particle size of the WI catalysts previously [5], and obtained an average particle diameter of 1.5 ± 0.5, 1.6 ± 0.5, and 1.7 ± 0.6 nm for the 0.5, 1, and 5 % Rh WI catalysts, respectively. On the 0.25% and 0.1% Rh WI catalysts (Fig. 1d and e, respectively), the Rh particles were too small to obtain a reliable size histogram.

Figure 1. High-angle annular dark-field scanning transmission electron microscopy

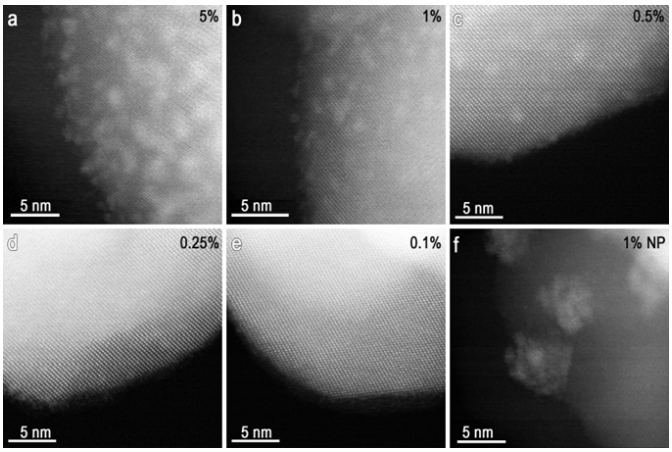

(HAADF-STEM) characterizations of fresh Rh/TiO_2 catalysts with varying loading.

Representative images of (a) 5 % Rh WI, (b) 1 % Rh WI, (c) 0.5 % Rh WI, (d) 0.25 % Rh WI, (e) 0.1% Rh WI, and (f) 1 % Rh NP.

However, we estimate that the 0.25% Rh WI catalyst contains Rh particles smaller than 1.0 nm, while those on the 0.1% Rh WI catalyst are smaller than 0.5 nm. Figure 1f shows a TEM image of the 1% Rh NP catalyst, and the corresponding particle size distribution histogram (Figure S1) indicates an average Rh particle size of 4.7 ± 0.7 nm.

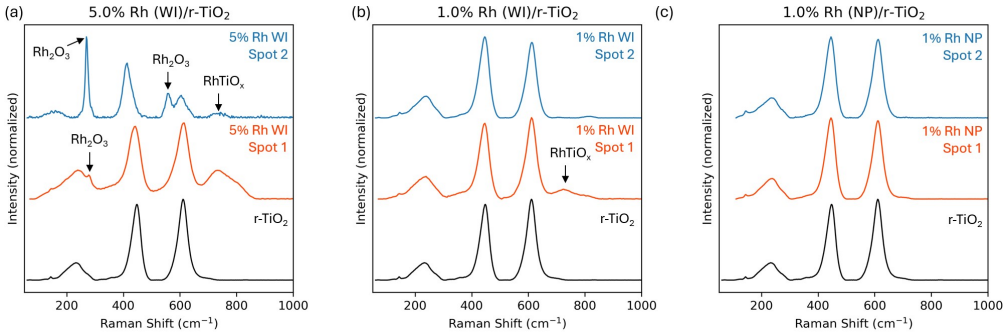

Figure 2. Raman measurements with 500 nm spatial resolution of the as prepared catalysts with high Rh loading, showing (a) 5% Rh WI, (b) 1% Rh WI and (c) 1% Rh NP. The black spectrum in each part is r-TiO_2 for reference, and the blue and orange spectra are representative spectra from two different areas on a catalyst grain.

To characterize the Rh oxidation state of the catalysts after their synthesis, we performed spatially resolved Raman measurements with 500 nm spatial resolution of the 5% and 1% Rh WI catalysts, the 1% Rh NP catalyst, and the pure rutile TiO_2 (r-TiO_2) support. The Raman spectra are shown in Figure 2. The pure r-TiO_2 shows three strong Raman bands at 232 cm^{-1}, 448 cm^{-1} and 615 cm^{-1}, and a weaker band at 143 cm^{-1}. Figure 2a compares the pure r-TiO_2 to the 5% Rh WI/r-TiO_2. Since the Rh content varied between different catalyst grains, representative spectra of two different grains are shown in the figure. Additional spectra from across the catalyst grains are shown in Figure S2a. The middle spectrum in Figure 2a shows less Rh-loading since the peaks originating from the r-TiO_2 remain clearly visible and experience some minor shifts in position. In addition to the bands originating from the r-TiO_2, two peaks are observed at 278 cm^{-1} and 733 cm^{-1}. The latter shows a shoulder towards 800 cm^{-1}. Wang et al. have assigned the band at ~280 cm^{-1} to Rh_2O_3 and the band at 730 cm^{-1} to $RhTiO_2$. [55] The top spectrum in Figure 2a shows a spectrum from a grain with a particularly high Rh loading. The 269 cm^{-1} Rh_2O_3 band is the strongest band in the spectrum. The 414 cm^{-1} and 556 cm^{-1}, also characteristic of Rh_2O_3, [55] are barely discernable as shoulders in the spectrum of the low Rh-loading but are clear peaks in the high Rh-loading spectrum. The r-TiO_2 features are small in the high Rh-loading grain and have slightly shifted to 604 cm^{-1} and a shoulder at ~440 cm^{-1}. There are also two weak peaks at ~150 cm^{-1} and ~730 cm^{-1}, indicating the formation of $RhTiO_x$ species where the Rh replaces Ti cation in the TiO_2 lattice.

Additional spatially resolved Raman spectra were recorded on the 1% Rh WI and the 1% Rh NP catalysts and are shown in Figures 2b and 2c, respectively. The spectra are largely dominated by the r-TiO_2 features, indicating this Rh loading is close to the detection limit of our Raman spectroscopy. A minor shift of the r-TiO_2 features by a few cm^{-1} could indicate some incorporation of Rh into the titania; only one spectrum of several collected showed a feature for $RhTiO_x$ in the 1% Rh WI sample (middle spectrum in Figure 2b). The spectra of the 1% Rh NP sample in Figure 2c are nearly identical to the r-TiO_2, with only a small shift in the support peaks observed (Figure S2c).

To assess the influence of Rh incorporation into the TiO_2 lattice, pair distribution function (PDF) analysis was applied to the wetness-impregnated catalysts. Figure 3a shows the corresponding radial PDF function G(r). All PDF data can be fit well using a single rutile TiO_2 phase, with no evidence of secondary crystalline phases. The data were further analyzed using a two-component non-negative matrix factorization (NMF) which deconvolute the complex dataset into distinct, additive parts. This procedure allows us to identify any secondary phases. This analysis results in the identification of two components: a component representing the rutile structure and a secondary component representing rutile with slightly expanded interatomic distances (Figure 3b). The fits of the PDFs as a function of catalyst loading are shown in Figure S3. There is an increase in the fraction of the second component (Figure 3c) with increasing wt% Rh. Contributions of Rh_2O_3 can be excluded due to the absence of any Rh_2O_3-related diffraction/PDF features and the highly consistent residuals across single-phase rutile fits at all Rh loadings (Figure S3). This result from the PDF analysis combined with the information from the Raman spectra (i.e. $RhTiO_x$ and shifted r-TiO_2 components) points to some Rh being incorporated into the titania lattice.

Figure 3. (a) Experimental PDF data of pure rutile TiO_2 and Rh-loaded catalysts (0.1-5 wt.%), with the highlighted low-r region for the two-component non-negative matrix factorization (NMF) analysis, showing the resulting (b) components and their (c) weights.

In situ characterization in O_2

Figure 4 shows APXPS measurements of the catalysts in $5x10^{-3}$ mbar O_2 atmosphere. To minimize any adventitious carbon on the samples, all catalysts were heated to 400 °C in O_2 for 30 min to remove the excess carbon and subsequently cooled in O_2. All APXPS data of the Rh 3d core level show the characteristic doublet structure resulting from the spin-orbit splitting of the 3d core level Typically, the area ratio of the doublet is determined by the fixed ratio based on spin-orbit splitting. However, for the Rh 3d core level the Koster Kroening effect broadens the $3d_{3/2}$ component and reduces its area. [56, 21]

The Raman measurements of the 5% Rh WI catalyst show two predominant chemical species of Rh are present in the catalyst, namely Rh_2O_3 and $RhTiO_x$. The two different oxidation states observed by XPS can thus be correlated to these two Rh species. Since Rh_2O_3 particles preferentially accumulate at the TiO_2 surface, while $RhTiO_x$ species are likely incorporated deeper into the TiO_2 lattice, their relative contributions to the XPS signal differ. Given the surface sensitivity of XPS, we therefore assign the larger, lower-binding-energy doublet to Rh_2O_3 and the smaller, higher-binding-energy doublet to $RhTiO_x$. In addition, the Rh_2O_3 component shifts to lower binding energy as the size increases, as shown in Table 1. This effect likely results from a charge transfer between the TiO_2 substrate to the particle. The smaller particles experience a greater shift than the larger particles. This effect has been reported earlier for Rh^0 [57, 18] and other metal clusters on single crystal TiO_2 surface [58, 59, 59].

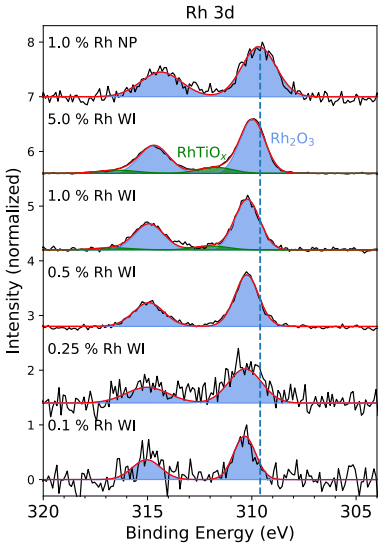

Figure 4. APXPS measurements of catalyst with different Rh particle size at 40 °C in $5x10^{-3}$ mbar O_2 after annealing the catalyst in O_2 atmosphere to 400 °C for 30 min. The spectrum of the 0.25% Rh WI catalyst was measured at the Advanced Light Source (ALS) with a photon energy of 880 eV. All other spectra were measured with the lab XPS instrument at the Center for function Nanomaterials (CFN) and an Al K_α source (1486.6 eV).

Theoretical characterization

To investigate the electronic effects responsible for the Rh 3d core-level shifts observed in the XPS measurements, we performed DFT calculations. Specifically, the Rh 3d core-level shifts (CLS) were calculated as a function of Rh cluster size for metallic Rh clusters supported on the TiO_2 surface. Metallic clusters were used to simplify the complexity of the calculations. Due to limitations of the unit cell size, clusters of 2, 4, 5, 7, and 8 atoms were chosen, and their structures were globally optimized (see SI for the details of the global optimization algorithm). Once the optimal cluster geometry was identified, the CLS for each atom was calculated (Figure 5). Along with the CLS, Bader charge analysis was used to determine the charge of each Rh atom in the cluster. Depictions of the optimized cluster geometries and Bader charges are available in the SI.

It was found that each cluster size donates electrons to the substrate acquiring an overall small positive charge. However, from the Bader charge analysis of clusters containing 4-8 atoms, only Rh atoms that are interfaced with the substrate are involved in charge transfer. Rh atoms that are shielded from the surface by a single mono layer of Rh atoms remain closer to neutral with an average Bader charge of -0.05. In contrast, Rh atoms in direct contact with the TiO_2 surface have an average Bader charge of + 0.065.the larger, lower-binding-energy doublet to Rh_2O_3 and the smaller, higher-binding-energy doublet to $RhTiO_x$.

Table 1. Rh oxide particle size obtained from TEM measurements and Rh $3d_{5/2}$ binding energies for Rh_2O_3 on the different catalysts.

Sample	Rh particle size (nm)	Rh $3d_{5/2}$ BE (eV)
1.0 % Rh NP	4.7 ± 0.7 [a]	309.7
5.0 % Rh WI	1.7 ± 0.6 [b]	310.0
1.0 % Rh WI	1.6 ± 0.5 [b]	310.2
0.5 % Rh WI	1.5 ± 0.5 [b]	310.2
0.25 % Rh WI	< 1.0 [c]	310.3
0.1 % Rh WI	< 0.5 [c]	310.4

a)The value is from the histogram in Figure S1. b) Values are from previous characterization in Ref [5]. c) Most Rh particles were too small to obtain a full histogram, so the largest size is given as a maximum.

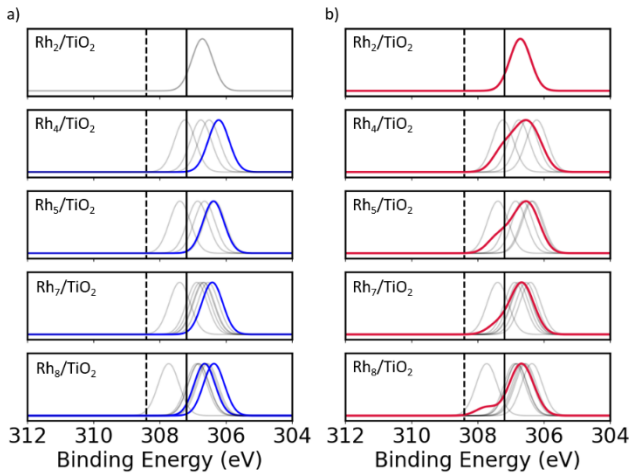

Figure 5. Rh 3d spectra of the Rh clusters as a function of size. Lines represent the computed CLS of bulk Rh_2O_3 (dashed) and Rh^0 (solid). Gray peaks represent the spectra of individual atoms. (a) On the left, blue spectra highlights the XPS of individual Rh atoms that are shielded from the TiO_2 surface by a single monolayer. (b) On the left, red spectra depicts the XPS superposition of Rh atoms for each cluster size.

Figure 5a demonstrates the effect of shielding on the CLS of individual atoms for each cluster size. Highlighted in blue are the predicted CLS of Rh atoms that are shielded by a monolayer of Rh atoms. Shielded Rh atoms have an average BE of 306.4 eV whereas interfacial Rh atoms (grey traces in Figure 5a) on average have a CLS of 306.8 eV. The interfacial Rh atoms exhibit higher binding energies due to the charge transfer with the substrate. The size dependence of the resulting XPS spectra can thus be attributed to the portion of the cluster that is in direct contact with the substrate. Smaller clusters will have on average more atoms in contact with surface which will result in a higher representation of interfacial character in the resulting XPS spectra. Conversely, large Rh clusters will have many more Rh atoms that are shielded from the surface. This transition from a majority of interfacial to bulk Rh atoms causes the peak to shift to lower binding energies as the size of Rh NPs increases. This trend is seen experimentally in Rh oxide binding energies in Table 1 and in metallic Rh discussed below.

In addition to the peak shift, different sized clusters are predicted to have different peak widths. Smaller clusters with more interfacial atoms and a diversity in the electronic structure of every individual atom, on average will have wider peaks. As the size of clusters increases, the increasing proportion of bulk Rh atoms will result in the narrowing of peaks. Figure 5b shows the superposition of all Rh binding energies of all Rh atoms in the cluster and indicates narrowing of the peaks as the size increases from Rh_4 to Rh_8. However, this systematic change in peak width is not observed in the experimental XPS spectra, which can likely be attributed to a distribution of Rh cluster sizes within each sample and to variations in surface orientation of the polycrystalline support.

In situ SAC formation in CO atmosphere

After determining the binding energy of Rh oxide particles, we recorded reference measurements for the binding energy of isolated Rh single atoms. These can readily be identified using IR spectroscopy with CO as a probe molecule. CO adsorbs as a carbonyl on Rh nanoparticles and as a *gem*-dicarbonyl on Rh SACs. These two different CO adsorption geometries have different vibrational frequencies. [60] Multiple IR studies of Rh/TiO_2 catalysts in CO atmosphere have shown that over an extended period of time, CO causes fragmentation of Rh particles into Rh single atoms. [30, 61, 62, 63] We used this phenomenon to obtain reference measurements for the XPS binding energy of Rh *gem*-dicarbonyl. The 1% Rh WI catalyst was initially annealed to 400 °C for 30 min in $9x10^{-3}$ mbar O_2 to remove most of the adventitious carbon from the surface. Subsequently, the sample was reduced by heating to 400 °C in $6.7x10^{-2}$ mbar H_2 for 30 min. Then the sample was cooled down to 80 °C in H_2 and once this temperature was reached, the H_2 was evacuated. Figure 6 shows the Rh 3d spectra of the catalyst measured with a photon energy of 880 eV in Figure 6a and 480 eV in Figure 6b, with the 480 eV photon energy being more surface sensitive. The two spectra at the top in Fig. 5a and b are the reference spectra of the catalyst post H_2 reduction. Both spectra show metallic Rh with a slightly asymmetric peak at a binding energy of 307.5 eV. The spectrum measured with higher photon energy has broader peaks due to the increased instrumental broadening at higher photon energy.

After measuring the reference spectra of the reduced catalyst, the sample was exposed to $1.3x10^{-1}$ mbar CO. The first Rh 3d spectrum was collected with 880 eV photon energy (Figure 6a) 10 min after starting the CO exposure. The spectrum shows that a new peak is beginning to form at 309.6 eV which we assign to Rh *gem*-dicarbonyl. Additionally, the metallic Rh peak shifts by 0.3 eV to higher binding energy (dashed red line). As discussed above, this shift could result from a change in Rh particle size. Alternatively, it could be caused by the adsorption of CO to the Rh nanoparticle and a charge transfer from the adsorbate. To further investigate this possibility, we performed additional DFT calculations on adsorption of CO to different sizes of metallic Rh clusters (see Figure S12). Our calculations indicate that the experimentally observed 0.3 eV shift of the metallic Rh in CO atmosphere is due to the adsorption of CO to the Rh nanoparticles.

The next Rh 3d spectrum was collected with 480 eV photon energy (Figure 6b) 30 min after starting the CO exposure, this spectrum also shows Rh *gem*-dicarbonyl and the same shift of metallic Rh. The Rh *gem*-dicarbonyl peak intensity is stronger in this spectrum due to the higher surface sensitivity of the lower photon energy and the longer exposure time to CO. The subsequent spectra in Figure 6 shows that more Rh single atom sites form over the next 60 min, and afterwards the system appears to reach an equilibrium state.

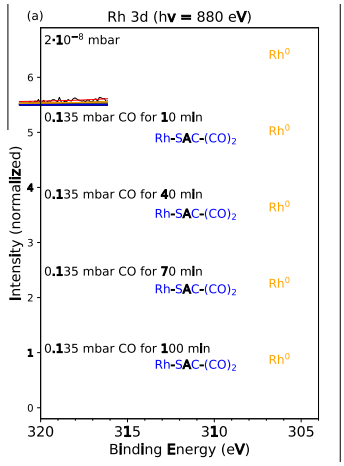

Figure 6. Rh 3d spectra of 1% Rh WI catalyst show the formation of Rh gem-dicarbonyl sites in a CO atmosphere (1x10^{-3} mbar) at 80 ºC collected with a photon energy of (a) 880 eV and (b) the more surface-sensitive 480 eV. The elapsed time when the data collection was started is indicated. The top spectrum in each panel is after annealing in H_2 to form Rh^0.

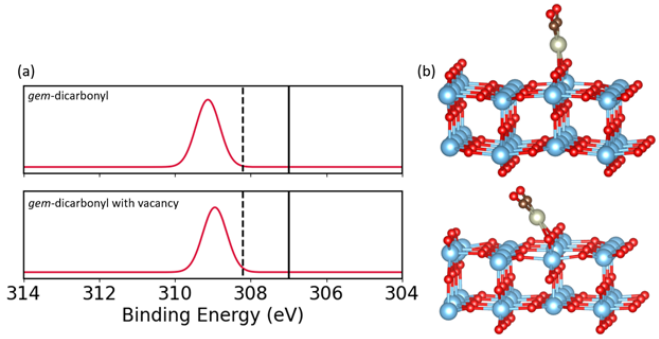

Figure 7. (a) Computed Rh 3d spectra of the gem-dicarbonyl with (bottom) and without (top) an oxygen vacancy in the lattice. Lines represent the computed CLS of bulk Rh_2O_3 (dashed) and Rh^0 (solid). (b) Global minimum structures of gem-dicarbonyls with (bottom) and without (top) vacancies in the lattice. Color code: O – red, Ti – blue, C – brown, Rh – silver.

Additionally, we studied possible structures and resulting CLS for Rh the *gem*-dicarbonyl with DFT. To search for the global minimum (GM) structure, 100 different structures were generated with the Rh *gem*-dicarbonyl at different initial locations and optimized using a machine learning potential (MLP) for rapid screening and then further optimized. A TiO_2 surface was also prepared with a bridging oxygen removed to see how the oxidation state of the surface changes the resulting CLS. In both cases, the Rh *gem*-dicarbonyls exhibits square planar geometry and bonding with two bridging oxygens which agrees with previous observations [64, 43]. The presence of the oxygen vacancy made very little difference in the Rh $3d_{5/2}$ binding energy which was calculated to be 309.3 eV for the surface with no vacancy and 309.1 eV for the surface with a vacancy. In comparison, the experimentally determined BE was found to be 309.6 eV. Additionally, a Bader charge of +0.71 was found for the Rh atom of the *gem*-dicarbonyl, and a charge of +0.72 was found for the case of a surface oxygen vacancy. The BE of the *gem*-dicarbonyl is found to be 0.7 eV higher than the computed BE of bulk Rh_2O_3, yet the computed Bader charge of Rh_2O_3 is calculated as +1.26. The remaining CLS of the *gem*-dicarbonyl that is not due to oxidation is likely due to strong π-backbonding of Rh with the CO ligands. Donation of electron density to the empty π^* CO orbitals draws electron density away from the orbitals close to the Rh core which reduces shielding and increases the core BE [65, 66].

In addition to the Rh single atom, Rh clusters of sizes 2, 4 and 7 atoms were also modelled under CO coverage (Figure S11). The results demonstrate that higher CO coverage induces larger charge transfer of the Rh clusters which shift the binding energy higher. This result is consistent with the experimentally observed trend of the Rh^0 peak shifting to higher BEs when going from UHV to CO atmosphere. Compared to the Rh single atom, clusters with high CO coverage do not exhibit as large of a CLS because the charge can distribute among the surrounding Rh atoms. Consequently, the CLS of the *gem*-dicarbonyl were found to be much higher than the any CLS of Rh atoms within clusters. This is in good agreement with the experimental observations in Figure 6, which show a well-defined gem-dicarbonyl peak at a binding energy much higher than that of any metallic Rh peaks.

To further investigate Rh nanoparticle fragmentation in a CO atmosphere, *in situ* XAS measurements were performed on the 0.5%RhWI/r-TiO_2 catalyst. The catalyst was treated using the same general procedure as in the APXPS measurements described above (see Methods for details). Figures 8a and 8b compare the XANES and EXAFS spectra of the pre-reduced sample before and after exposure to 10% CO/He for 1 h at 80 °C. After the reduction step and prior to CO exposure, Rh is predominantly reduced, as indicated by the XANES spectrum (Figure 8a). Modeling of the EXAFS data shows that the best fit consists primarily of a Rh–Rh scattering path (CN_{Rh-Rh} = 6.6 ± 0.6), with a minor Rh–O contribution (CN_{Rh-O} = 0.5 ± 0.2) (Table S5, Figures 8c–d), which is attributed to interfacial oxygen species. After 1 h of exposure to flowing 10% CO/He at 80 °C, clear changes are observed in the XANES (Figure 8a). The Fourier-transform EXAFS spectrum shows a decrease in the Rh–Rh peak accompanied by the emergence of a Rh–O/C peak at ~1.2 Å (Figure 8b). The best-fit EXAFS model reveals a decrease in the Rh–Rh coordination number to 4.0 ± 0.5, consistent with a reduction in the average Rh nanoparticle size (Table S5, Figures 8 e-f). Inclusion of four additional scattering paths—Rh–C and Rh–O single-scattering, together with Rh–C–O and Rh–C–O–C multiple-scattering paths, associated with CO adsorbed on Rh—significantly improves the fit (Table S5-6, Figures 8e-f, S5).

These results support CO-induced fragmentation of Rh nanoparticles, consistent with the XPS observations, as increased dispersion of Rh leads to the formation of smaller clusters or single atoms which make it capable to detect binding CO ligands by EXAFS.

Discussion

This study demonstrates that APXPS provides qualitative insight into changes in Rh cluster size for both oxidized and reduced Rh particles, as evidenced by size-dependent shifts in the Rh 3d core-level binding energies. By collecting Rh 3d core level spectra under different atmospheres and coupling with *ex situ* Raman spectroscopy, PDF and TEM measurements, it was possible to deconvolute size-dependent charge transfer from oxidation state changes. It was observed that smaller Rh particles experience stronger interaction with the supportwith the support than larger particles as can be observed by shifts of the APXPS binding energy and accompanying DFT calculations. These shifts could be observed for oxidized and metallic Rh particles. The Rh 3d binding energy of single atoms in the *gem*-dicarbonyl state were identified, with structural confirmation from *in situ* XANES and EXAFS. Table 2 summarizes the measured binding energies of the different Rh species on rutile TiO_2. A comparison of the Rh 3d spectra of Rh_2O_3, Rh *gem*-dicarbonyl and metallic Rh is shown in the Figure S13.

Table 2. Summary of experimentally obtained XPS binding energies of the Rh $3d_{5/2}$ core level for different oxidation states of nanostructured Rh species

	Rh $3d_{5/2}$ BE (eV)
Rh^0 cluster	307.4 – 307.8
Rh-SAC-$(CO)_2$	309.6
Rh_2O_3	310.0 – 310.3 (WI) 309.5 (4.7 nm NP)
$RhTiO_x$	311.7

Previous studies on single crystal TiO_2 investigated the charge transfer with Rh clusters in UHV and observed a similar size-depended on charger transfer effects as in the presented study. [57, 18] For these metallic Rh clusters binding energy shifts of 0.7 eV have been reported between 0.6 nm and 3.1 nm metallic Rh clusters and an additional 0.1 eV shift between the 3.1 nm clusters and Rh thin films. [18] For the Rh_2O_3 particles, we observed a 0.8 eV shift between the smaller than 0.5 nm 0.1 % Rh WI catalysts and the 4.7 nm 1.0% Rh NPs, which is in good agreement with the previous results for metallic Rh clusters on single crystalline TiO_2. Similar size dependent energy shifts have been reported for Pt and Pd clusters on TiO_2 single crystals. [58, 59, 67, 59, 67] The DFT calculations presented in Figure 5 indicate an analogous charge transfer effect in the current system and reveal that the charge transfer is only experienced by Rh atoms in direct contact with the TiO_2 support while other Rh atoms are electronically shielded.

When studying size-dependent binding energy shifts of nanoparticles on oxide supports, there is a volume of literature ascribing shifts to either charge transfer, also called initial state effects, or final state effects. Materials with high electron mobility efficiently screen the core hole created during the photoemission process, whereas high-bandgap oxide supports with low electron mobility screen these core holes less effectively. This reduced screening gives rise to additional binding energy shifts associated with final-state effects. [68] However, there are few studies that carefully disentangle the contributions from each of these effects because it is experimentally challenging. [69] On consistent theme in literature is that oxide supports with larger band gaps and lower defect densities, such as SiO_2 or Al_2O_3. TiO_2-supported systems are more strongly influenced by charge-transfer effects than by final-state effects. [69] due to efficient core-hole screening from higher electron mobility. For this reason, we further investigated charge transfer effects with DFT and realize that final state effects cannot be excluded. Overall, the size-dependent binding energy shifts observed by APXPS can be used to qualitatively track particle size under operando conditions.

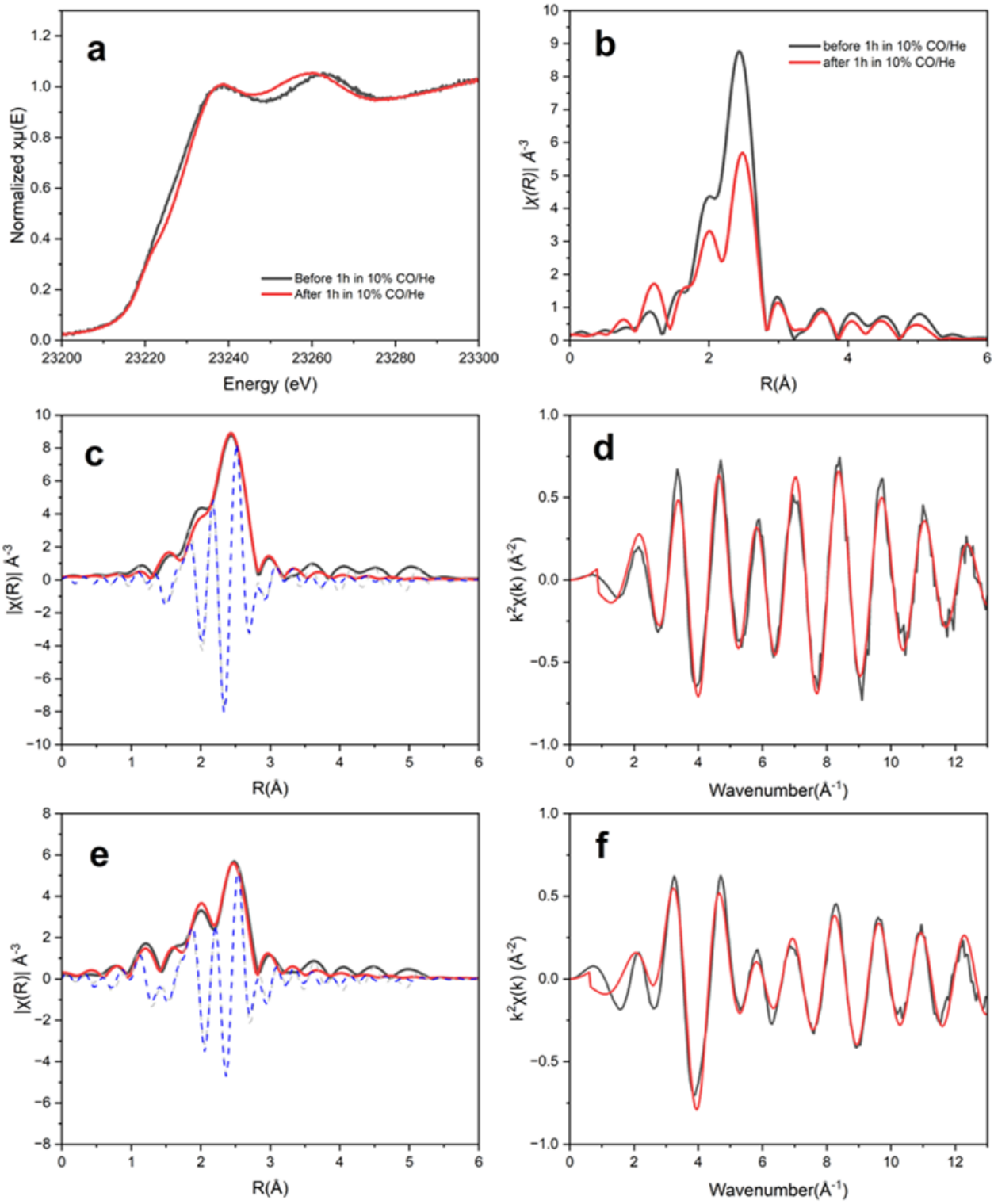

Figure 8. Comparison of (a) XANES and (b) Fourier-transform EXAFS spectra of 0.5%RhWI/r-TiO_2 before and after 1 hour exposure to 10%CO/He at 80°C. Results of EXAFS analysis characterizing 0.5%RhWI/r-TiO_2 sample (c-d) before and (e-f) after 1 hour exposure to 10%CO/He at 80°C in R-space: the experimental data and corresponding fit in magnitude (black and red lines, respectively) and in imaginary space (grey and blue lines, respectively); and in k-space: the experimental data and corresponding fit, black and red lines, respectively. R range: 1- 3.2 Å, k-range 3.0-12.0 Å-1.

The second part of this manuscript focuses on the fragmentation of metallic Rh particles under a CO atmosphere. Fragmentation was observed experimentally using APXPS and XAS. APXPS measurements revealed a shift in the binding energy of metallic Rh upon exposure to CO. Through additional DFT calculations, we demonstrated that this shift originates from CO adsorption on the Rh nanoparticles.

The formation of Rh *gem*-dicarbonyl species from metallic Rh particles on polycrystalline rutile TiO_2 powder under CO atmosphere has been previously investigated in a prior *in vacuo* XPS study [30]. Specifically, the study reported metallic Rh at 306.6 eV and Rh *gem*-dicarbonyl at 312.0 eV. The reported binding energies differ considerably from our measurements, likely due to two main factors. Their sample reduction was conducted at a considerably higher pressure (100 Torr) than the current study (6.7×10^{-2} mbar, or 0.05 Torr) and moved to the analysis chamber without exposure to air; the higher-pressure treatment could have resulted in larger Rh particles. Additionally, the spectra reported here are calibrated to the Ti 2p signal, whereas the previous study used the C 1s peak for binding energy calibration. Calibration to the C 1s signal can introduce errors, as adventitious carbon may alter its chemical state under strong oxidative or reductive conditions. By measuring the dynamics of the Rh oxidation *in situ*, the current study offers robust assignment of the Rh $3d_{5/2}$ binding energies.

Ex situ low-pressure studies on single-crystal TiO_2 have reported Rh *gem*-dicarbonyl species at 309.1 eV [10] and 310.1 eV [66], respectively. These discrepancies in the reported binding energies may, as well, result from differences in the energy calibration procedures used in the XPS measurements. Reference [66] states that the XPS spectra were calibrated using a gold foil, which is suitable for calibrating the X-ray photon energy but does not account for possible charging effects of the Rh/TiO_2 sample during measurement, potentially leading to inaccurate binding energy determination. Reference [10] does not elaborate on its energy calibration method, making direct comparison to other measurements difficult. In the current study, the Ti $2p_{3/2}$ peak is used as a reference for binding energy calibration. Additionally, charging effects were mitigated by preparing thin pellets of sample on a metal substrate, heating the sample, and collecting data under gas pressures. Using this rigorous calibration method, charge mitigation techniques, carefully selected reference measurements, and complementary spectroscopy techniques, we posit that we have determined accurate binding energies that will enable future studies to distinguish between oxidation states of these dynamic catalysts.

The previous literature reports focused on model systems of well-defined nanostructure metal species on single crystalline surfaces. Our study builds on this foundation to follow nanostructured Rh species on a polycrystalline powder TiO_2 support, which is a step towards bridging the materials gap for industrially relevant catalysts. Additionally, our reference measurements and *ex situ* characterizations helped deconvolute binding energy shifts due to Rh structural changes from dynamic oxidation state changes. Insight into the magnitude of binding energy shifts in Rh on r-TiO_2 should help guide future studies in Rh 3d spectral assignment, where the literature has offered a range of assignments, possibly due to the effects that we describe. This allows us to use APXPS as an indirect way to monitor particle size changes under *in situ* conditions for TiO_2-supported catalysts from the Pt-group. Our results lay the foundation for future *in situ* studies of Rh fragmentation and sintering and *operando* studies of catalytic reactions.

Conclusions

In this work, we investigated the XPS binding energies of nanoscale Rh species on polycrystalline rutile TiO_2 powder as a function of Rh particle size for Rh_2O_3 under *in situ* conditions. We found that charge exchange between Rh and its support leads to shifts in binding energy, with smaller particles exhibiting larger shifts due to stronger charge transfer with the support. These size effects were disentangled from changes in Rh oxidation state through comparison with ex situ Raman spectroscopy, PDF, and TEM measurements, as well as correlative XANES and EXAFS analysis. The experimentally observed size-dependent charge transfer trends of reduced Rh and Rh under CO pressure are further supported by DFT calculations. These findings demonstrate that APXPS can serve as an indirect yet powerful method to qualitatively track changes in Rh particle size and oxidation state changes under *operando* conditions, providing valuable insight into structure–function relationships in these catalytic systems.

Author contributions

S. M. G. – conceptualization, investigation, writing – original draft, writing- review & editing; J.E. - investigation, writing – original draft; X. C. – investigation, formal analysis; A. K. – investigation, writing – original draft, Z. C. - investigation, writing – original draft, Y. L. – methodology, investigation; S.H. – resources, writing – original draft; J. H. – resources, writing – original draft; E. K. S.- resources, S. B. – resources; J. N. – investigation; M. B. – resources, S. N. – resources; P. C. – supervision; M. C. – supervision; A. S. H. – resources, writing – review & editing; S. R. B. – resources, funding acquisition, supervision, writing – review & editing; S. T. – resources; J. C. Y. – supervision; A. A. – conceptualization, writing – review & editing, supervision; A. R. H. – conceptualization, supervision, resources, writing – review & editing

Conflicts of interest

There are no conflicts to declare.

Data availability

The data supporting this article have been included as part of the Supplementary Information. Supplementary information: Tables S1 – S6, TEM histogram, additional Raman spectra, additional XPS data, PDF fits, EXAFS analysis of Rh foil, and further computational details. See DOI: [URL – format https://doi.org/DOI]

Acknowledgements

S.M.G. gratefully acknowledges Florian Kraushofer for the insightful discussions during the 2025 GRC on Chemical Reactions at Surfaces, which contributed to the development of this work.

The work was supported by the Division of Chemical Sciences, Geosciences, and Biosciences, Office of Basic Energy Sciences, U.S. Department of Energy (DOE) as part of the Accelerate Innovations in Emerging Technologies initiative FWP 101064. This research used the Proximal Probes and Electron Microscopy Facilities of the Center for Functional Nanomaterials, at Brookhaven National Laboratory, which is supported by the US Department of Energy, Office of Basic Energy Sciences, under Contract No. DE-SC0012704. This research used resources of the Advanced Light Source, a U.S. DOE Office of Science User Facility under contract no. DE-AC02-05CH11231. Use of the Stanford Synchrotron Radiation Light Source, SLAC National Accelerator Laboratory, is supported by the U.S. Department of Energy, Office of Science, Office of Basic Energy Sciences under Contract No. DE-AC02-76SF00515. This research used beamline 28-ID-1 of the National Synchrotron Light Source II, a U.S. Department of Energy (DOE) Office of Science User Facility operated for the DOE Office of Science by Brookhaven National Laboratory under Contract No. DE-SC0012704. Computations were performed on the DOE National Energy Research Scientific Computing Center (NERSC).

Notes and references

[1] R. M. Palomino, J. W. Magee, J. Llorca, S. D. Senanayake and M. G. White, "The effect of Fe-Rh alloying on CO hydrogenation to C_{2+} oxygenates," *Journal of Catalysis,* vol. 329, pp. 87-94, 2015.

[2] É. Novák, K. Fodor, T. Szailer, A. Oszkó and A. Erdöhelyi, "CO_2 hydrogenation on Rh/TiO_2 previously reduced at different temperatures," *Topics in Catalysis,* vol. 20, no. 1-4, pp. 107-117, 2002.

[3] Y. Yang, J. Liu, F. Liu and D. Wu, "Reaction mechanism of CO_2 methanation over Rh/TiO_2 catalyst," *Fuel,* vol. 276, no. April, p. 118093, 2020.

[4] Y. Tang, C. Asokan, M. Xu, G. W. Graham, X. Pan, P. Christopher, J. Li and P. Sautet, "Rh single atoms on TiO_2 dynamically respond to reaction conditions by adapting their site," *Nature Communications,* vol. 10, pp. 1-10, 2019.

[5] E. K. Schroeder, S. Hong, X. Chen, A. S. Hoffman, Z. Chen, A. Khan, G. D. Barber, S. Bac, R. M. Rioux, J. Yang, C. J. Tassone, S. R. Bare and P. Christopher, "Structural Evolution and Stability of Rh/TiO_2 Catalysts under CO_2 Hydrogenation Conditions: Influence of the Initial Rh Structure," *ACS Catalysis,* pp. 12133-12147, 2025.

[6] L. Yang, J. Wang, T. Liu, H. He, X. Li, X. Zhang and J. Li, "Synergistic Catalysis of Rh Single-Atom and Clusters Supported on TiO_2 Nanosheet Array for Highly Efficient Removal of CO and NO_x," *Small Structure,* vol. 5, p. 2400230, 2024.

[7] R. C. A. E. T. R. Zanella, "Influence of the Preparation Method of Au , Pd , Pt , and Rh/TiO_2 Nanostructures and Their Catalytic Activity on the CO Oxidation at Low Temperature," *Topics in Catalysis,* vol. 65, no. 7, pp. 798-816, 2022.

[8] J. C. Matsubu, V. N. Yang and P. Christopher, "Isolated metal active site concentration and stability control catalytic CO_2 reduction selectivity," *Journal of the American Chemical Society,* vol. 137, no. 8, pp. 3076-3084, 2015.

[9] J. C. Matsubu, S. Zhang, L. DeRita, N. S. Marinkovic, J. G. Chen, G. W. Graham, X. Pan and P. Christopher, "Adsorbate-mediated strong metal-support interactions in oxide-supported Rh catalysts," *Nature Chemistry,* vol. 9, no. 2, pp. 120-127, 2017.

[10] B. Hayden, A. King and M. A. Newton, "The reaction of hydrogen with TiO2(110) supported rhodium gem-dicarbonyl," *Surface Science,* vol. 397, pp. 306-313, 1998.

[11] F. C. Meunier, "Relevance of IR Spectroscopy of Adsorbed CO for the Characterization of Heterogeneous Catalysts Containing Isolated Atoms," *Journal of Physical Chemistry C,* vol. 125, no. 40, pp. 21810-21823, 2021.

[12] J. Hulva, M. Meier, R. Bliem, Z. Jakub, F. Kraushofer, M. Schmid, U. Diebold, C. Franchini and G. S. Parkinson, "Unraveling CO adsorption on model single-atom catalysts," *Science,* vol. 371, no. 6527, pp. 375-379, 2021.

[13] M. J. Hülsey, B. Zhang, Z. Ma, H. Asakura, D. A. Do, W. Chen, T. Tanaka, P. Zhang, Z. Wu and N. Yan, "In situ spectroscopy-guided engineering of rhodium single-atom catalysts for CO oxidation," *Nature Communications,* vol. 10, no. 1, 2019.

[14] D. McClure, S.M. and Lundwall, M. J. and Goodmann, "Planar oxide supported rhodium nanoparticles as model catalysts," *PNAS,* vol. 108, no. 3, pp. 931-936, 2011.

[15] H. Khan, A. S. Yerramilli, A. D'Oliveira, T. L. Alford, D. C. Boffito and G. S. Patience, "Experimental methods in chemical engineering: X-ray diffraction spectroscopy—XRD," *Canadian Journal of Chemical Engineering,* vol. 98, no. 6, pp. 1255-1266, 2020.

[16] T. Li, A. J. Senesi and B. Lee, "Small Angle X-ray Scattering for Nanoparticle Research," *Chemical Reviews,* vol. 116, no. 18, pp. 11128-11180, 2016.

[17] J. R. Jinschek, "Advances in the environmental transmission electron microscope (ETEM) for nanoscale in situ studies of gas-solid interactions," *Chemical Communications,* vol. 50, no. 21, pp. 2696-2706, 2014.

[18] L. Óvári and J. Kiss, "Growth of Rh nanoclusters on TiO_2(110): XPS and LEIS studies," *Applied Surface Science,* vol. 252, no. 24, pp. 8624-8629, 2006.

[19] M. A. Sharp, C. J. Lee, M. Mahapatra, R. S. Smith, B. D. Kay and Z. Dohnálek, "Preparation and Characterization of Model Homotopic Catalysts: Rh Adatoms, Nanoparticles, and Mixed Oxide Surfaces on Fe_3O_4(001)," *Journal of Physical Chemistry C,* vol. 126, no. 34, pp. 14448-14459, 2022.

[20] C. J. Lee, M. A. Sharp, B. A. Jackson, M. Mahapatra, S. Raugei, M.-s. Lee, B. D. Kay and Z. Dohn, "Dynamic Activation of Single-Atom Catalysts by Reaction Intermediates : Conversion of Formic Acid on Rh / Fe_3O_4(001)," *ACS Catalysis,* vol. 4, no. 001, 2024.

[21] Y. Abe, K. Kato and K. Sasaki, "Rhodium and Rhodium Oxide Thin Films Characterized by XPS," *Surface Science Spectra,* vol. 8, pp. 117-125, 2001.

[22] S. Blomberg, E. Lundgren, R. Westerström, E. Erdogan, N. M. Martin, A. Mikkelsen, J. N. Andersen, F. Mittendorfer and J. Gustafson, "Structure of the Rh_2O_3(0001) surface," *Surface Science,* vol. 606, no. 17-18, pp. 1416-1421, 2012.

[23] K. Kato, Y. Abe, M. Kawamura and K. Sasaki, "Preparation of RhO2 thin films by reactive sputtering and their characterizations," *Japanese Journal of Applied Physics, Part 1: Regular Papers and Short Notes and Review Papers,* vol. 40, no. 4 A, pp. 2399-2402, 2001.

[24] L. S. Kibis, A. I. Stadnichenko, S. V. Koscheev, V. I. Zaikovskii and A. I. Boronin, "XPS Study of Nanostructured Rhodium Oxide Film Comprising Rh^{4+} Species," *Journal of Physical Chemistry C,* vol. 120, no. 34, pp. 19142-19150, 2016.

[25] K. T. Jacob and D. Prusty, "Thermodynamic properties of RhO2," *Journal of Alloys and Compounds,* vol. 507, no. 1, pp. 17-20, 2010.

[26] O. Muller and R. Roy, "Formation and stability of the platinum and rhodium oxides at high oxygen pressures and the structures of Pt_3O_4, β-PtO_2 and RhO_2," *Journal of The Less-Common Metals,* vol. 16, no. 2, pp. 129-146, 1968.

[27] B. Hayden, Chemisorption and Reactivity on Supported Clusters and Thin Films, 1997, pp. 215-237.

[28] S. Suárez, M. Yates, A. L. Petre, J. A. Martín, P. Avila and J. Blanco, "Development of a new Rh/TiO_2-sepiolite monolithic catalyst for N_2O decomposition," *Applied Catalysis B: Environmental,* vol. 64, no. 3-4, pp. 302-311, 2006.

[29] G. Munuera, A. Gonyalez-Elipe, J. Espinos and A. Navio, "XPS characterization of oxygenated species in TiO_2 and Rh/TiO_2 photocatalysts," *Journal of Molecular Structure,* vol. 143, pp. 227-230, 1986.

[30] D. A. Buchanan, M. E. Hernandez, F. Solymosi and M. J. White, "CO-Induced Structural Changes of Rh on TiO_2 Support," *Jornal of Catalysis,* vol. 125, pp. 456-466, 1990.

[31] D. E. Starr, Z. Liu and M. Ha, "Investigation of solid/vapor interfaces using ambient pressure X-ray photoelectron spectroscopy," *Chemical Society Reviews,* vol. 42, pp. 5833-5857, 2013.

[32] J. J. Velasco-Vélez, V. Pfeifer, M. Hävecker, R. Wang, A. Centeno, A. Zurutuza, G. Algara-Siller, E. Stotz, K. Skorupska, D. Teschner, P. Kube, P. Braeuninger-Weimer, S. Hofmann, R. Schlögl and A. Knop-Gericke, "Atmospheric pressure X-ray photoelectron spectroscopy apparatus: Bridging the pressure gap," *Review of Scientific Instruments,* vol. 87, no. 5, 2016.

[33] P. Amann, D. Degerman, M. T. Lee, J. D. Alexander, M. Shipilin, H. Y. Wang, F. Cavalca, M. Weston, J. Gladh, M. Blom, M. Björkhage, P. Löfgren, C. Schlueter, P. Loemker, K. Ederer, W. Drube, H. Noei, J. Zehetner, H. Wentzel, J. Åhlund and A. Nilsson, "A high-pressure x-ray photoelectron spectroscopy instrument for studies of industrially relevant catalytic reactions at pressures of several bars," *Review of Scientific Instruments,* vol. 90, no. 10, 2019.

[34] P. H. Chung, A. C. Yang, C. Zhou, J. Oh, M. Homer, C. Lizandara-Pueyo, Y. Li and M. Cargnello, "Aqueous-Phase Synthesis of Pt and PGM-Based Nanocrystals with a Controllable Size," *Crystal Growth and Design,* vol. 24, no. 24, pp. 10413-10422, 12 2024.

[35] L. Zhang, D. A. Cullen, P. Zhai and K. Ding, "Adsorption of Colloidal Metal Nanoparticles via Solvent Engineering," *ACS Catalysis,* vol. 10, no. 3, pp. 2378-2383, 2 2020.

[36] M. E. Grass, P. G. Karlsson, F. Aksoy, M. Lundqvist, B. Wannberg, B. S. Mun, Z. Hussain and Z. Liu, "New ambient pressure photoemission endstation at advanced light source beamline 9.3.2," *Review of Scientific Instruments,* vol. 81, no. 5, 5 2010.

[37] C. N. Eads, J. Q. Zhong, D. Kim, N. Akter, Z. Chen, A. M. Norton, V. Lee, J. A. Kelber, M. Tsapatsis, J. A. Boscoboinik, J. T. Sadowski, P. Zahl, X. Tong, D. J. Stacchiola, A. R. Head and S. A. Tenney, "Multi-modal surface analysis of porous films under operando conditions," *AIP Advances,* vol. 10, no. 8, 2020.

[38] N. Fairely, "CasaXPS Manual 2.3. 15 Getting started with CasaXPS," *Casa Software Ltd,* pp. 1-177, 2009.

[39] G. Kresse and D. Joubert, "From ultrasoft pseudopotentials to the projector augmented-wave method," *Physical Review B,* vol. 59, no. 3, pp. 1758-1775, 1999.

[40] J. P. Perdew, K. Burke and M. Ernzerhof, "Generalized Gradient Approximation Made Simple," *Physical Review Letters,* vol. 77, no. 18, pp. 3865-3868, 1996.

[41] S. Dudarev, G. Bottom, S. Savrosav, C. Humphreys and A. Sutton, "Electron-energy-loss spectra and the structural stability of nickel oxide: An LSDA+U study," *Physical Review B,* vol. 57, no. 3, pp. 1505-1509, 1998.

[42] M.-A. Ha and A. N. Alexandrova, "Oxygen Vacancies of Anatase(101): Extreme Sensitivity to the Density Functional Theory Method," *Journal of Chemical Theory and Computation,* vol. 12, no. 6, pp. 2889-2895, 2016.

[43] Y. Tang, C. Asokan, M. Xu, G. W. Graham, X. Pan, P. Christopher, J. Li and P. Sautet, "Rh single atoms on TiO_2 dynamically respond to reaction conditions by adapting their site," *Nature Communications,* vol. 10, no. 1, p. 4488, 2019.

[44] L. Köhler and G. Kresse, "Density functional study of CO on Rh(111)," *Physical Review B,* vol. 70, no. 16, p. 165405, 2004.

[45] I. e. a. Batatia, "A foundation model for atomistic materials chemistry," *The Journal of Chemical Physics,* vol. 163, no. 18, 2025.

[46] I. Batatia, S. Batzner, D. P. Kovács, A. Musaelian, G. N. C. Simm, R. Drautz, C. Ortner and B. Kozinsky, "The design space of E(3)-equivariant atom-centred interatomic potentials," *Nature Machine Intelligence,* vol. 7, no. 1, pp. 56-67, 2025.

[47] Y. Lee, X. Chen, S. M. Gericke, M. Li, D. N. Zakharov, A. R. Head, J. C. Yang and A. N. Alexandrova, "Machine-Learning-Driven Exploration of Surface Reconstructions of Reduced Rutile TiO_2," *Angewandte Chemie International Edition,* vol. 64, no. 26, 2025.

[48] Z. Zhang, W. Gee, R. H. Lavroff and A. N. Alexandrova, "GOCIA: a grand canonical global optimizer for clusters, interfaces, and adsorbates," *Physical Chemistry Chemical Physics,* vol. 27, no. 2, pp. 696-706, 2025.

[49] B. H. Toby and R. B. Von Dreele, "GSAS-II: The genesis of a modern open-source all purpose crystallography software package," *Journal of Applied Crystallography,* vol. 46, no. 2, pp. 544-549, 2013.

[50] X. Qiu, J. W. Thompson and S. J. Billinge, "PDFgetX2: A GUI-driven program to obtain the pair distribution function from X-ray powder diffraction data," *Journal of Applied Crystallography,* vol. 37, no. 4, p. 678, 2004.

[51] D. O'Nolan, H. Zhao, Z. Chen, A. Grenier, M. L. Beauvais, M. A. Newton, T. M. Nenoff, P. J. Chupas and K. W. Chapman, A multimodal analytical toolkit to resolve correlated reaction pathways: The case of nanoparticle formation in zeolites, vol. 12, 2021, pp. 13836-13847.

[52] C. H. Liu, C. J. Wright, R. Gu, S. Bandi, A. Wustrow, P. K. Todd, D. O'Nolan, M. L. Beauvais, J. R. Neilson, P. J. Chupas, K. W. Chapmanc and S. J. Billinge, "Validation of non-negative matrix factorization for rapid assessment of large sets of atomic pair distribution function data," *Journal of Applied Crystallography,* vol. 54, pp. 768-775, 2021.

[53] B. Ravel and M. Newville, "ATHENA, ARTEMIS, HEPHAESTUS: Data analysis for X-ray absorption spectroscopy using IFEFFIT," *Journal of Synchrotron Radiation,* vol. 12, no. 4, pp. 537-541, 2005.

[54] A. S. Hoffman, J. A. Singh, S. F. Bent and S. R. Bare, "In situ observation of phase changes of a silica- supported cobalt catalyst for the Fischer–Tropsch process by the development of a synchrotron- compatible in situ/operando powder X-ray diffraction cell," *Journal of Synchrotron Radiation,* vol. 25, no. 6, pp. 1673-1682, 2018.

[55] J. Wang, K. Liu, B. Zhang, Y. Qiu, Y. Xiang, W. Lin, B. Yang, B. Li and G. Ma, "Doping Rh into TiO_2 as a visible-light-responsive photocatalyst: The difference between rutile and anatase," *Applied Physics Letters,* vol. 119, p. 213901, 2021.

[56] L. Köver, J. Toth and A. Itoh, "An experimental methode for resolution calibration of electron spectrometers," *Acta Physica Hungaria,* vol. 65, no. 2, pp. 217-228, 1989.

[57] A. Berkó, I. Ulrych and K. C. Prince, "Encapsulation of Rh nanoparticles supported on TiO_2(110)-(1 × 1) surface: XPS and STM studies," *Journal of Physical Chemistry B,* vol. 102, no. 18, pp. 3379-3386, 1998.

[58] H.-P. Steinrück, F. Pesty, L. Zhang and T. E. Madey, "Ultrathin films of Pt on TiO_2(110): Growth and chemisorption-induced surfactant effects," *Physical Review,* vol. 51, no. 4, p. 2427, 1995.

[59] F. S. Roberts, S. L. Anderson, A. C. Reber and S. N. Khanna, "Initial and final state effects in the ultraviolet and X-ray photoelectron spectroscopy (UPS and XPS) of size-selected Pd_n clusters supported on TiO_2(110)," *Journal of Physical Chemistry C,* vol. 119, no. 11, pp. 6033-6046, 2015.

[60] A. C. Yang and C. W. Garland, "Infrared studies of carbon monoxide chemisorbed on Rhodium," *Journal of Physical Chemistry,* vol. 61, pp. 1504-1513, 1957.

[61] H. F. J. Van't Bilk, J. B. A. D. Van Zon, T. Huizinga, J. C. Vis, D. C. Koningsberger and R. Prlns, "Extended X-ray Absorption Fine Structure Spectroscopy Study of a Highly Dispersed Rh/Al_2O_3 Catalyst: The Influence of CO Chemisorption on the Topology of Rhodium," *J. Phys. Chem,* vol. 87, pp. 2264-2267, 1983.

[62] H. F. J. Van't Bilk, J. B. A. D. van Zon, T. Huizinga, J. C. Vis, D. C. Koningsberger and R. Prins, "Structure of Rhodium in an Ultradispersed Rh/Al_2O_3 Catalyst," *J. Am. Chem. Soc.,* vol. 107, no. 11, pp. 3139-3147, 1984.

[63] H. F. J. Van't Blik, J. B. A. D. Van Zon, D. C. Koningsberger and R. Prins, "EXAFS determination of the change in the structure of rhodium in highly dispersed Rh/γ-Al2O3 catalysts after CO and/or H2 adsorption a different temperatures," *Journal of Molecular Catalysis,* vol. 25, pp. 379-396, 1984.

[64] C. Wang, P. Sombut, L. Puntscher, Z. Jakub, M. Meier, J. Pavelec, R. Bliem, M. Schmid, U. Diebold, C. Franchini and G. S. Parkinson, "CO-Induced Dimer Decay Responsible for Gem-Dicarbonyl Formation on a Model Single-Atom Catalyst," *Angewandte Chemie International Edition,* vol. 63, no. 16, 2024.

[65] H. W. Chen and W. L. Jolly, "An XPS study of the relative pi-acceptor abilities of the nitrosyl and carbonyl," *Inorganic Chemistry,* vol. 18, no. 9, pp. 2548-2551, 1979.

[66] M. Eder, F. J. Lewis, J. I. Hütner, P. Sombut, D. Rath, J. Balajka, M. Wagner, M. Meier, U. Diebold, M. Schmid, F. Libisch, J. Pavelec and G. S. Parkinson, "Multi-Technique Characterization of Rhodium Gem- Dicarbonyls on TiO_2(110)," *Chemical Science,* 2025.

[67] F. Kraushofer, M. Krinninger, M. de la Higuera-Domingo, L. Falling, L. Strauss, S. Kaiser, M. Salehi, G. Anand, V. P. Dieste, M. Blum and B. A. J. Lechner, "Pt Particles on a Dynamic TiO_2 Support in Near-Ambient Conditions–Disentangling Size, Pressure, and Support Effects," *Journal of the American Chemical Society,* vol. 147, no. 43, pp. 39846-39859, 10 2025.